Structure and Transport Properties of Nanostructured Materials

C. G. Sonwane* and Q. Li

National Institute of Standards and Technology, 836/221, 100 Bureau Drive, Gaithersburg, Maryland 20899, Department of Chemical Engineering, University of California Berkeley, 201 Gilman Hall, Berkeley, California 94720, and UMCP/NIST Co-Laboratory on NanoParticle Based Manufacturing and Metrology, University of Maryland, College Park, Maryland 20742

In the present manuscript, we have presented the simulation of nanoporous aluminum oxide using a molecular-dynamics approach with recently developed dynamic charge transfer potential using serial/parallel programming techniques (Streitz and Mintmire *Phys. Rev. B* **1994,** *50,* 11996). The structures resembling recently invented ordered nanoporous crystalline material, MCM-41/SBA-15 (Kresge et al. *Nature* **1992,** *359,* 710), and inverted porous solids (hollow nanospheres) with up to 10 000 atoms were fabricated and studied in the present work. These materials have been used for separation of gases and catalysis. On several occasions including the design of the reactor, the knowledge of surface diffusion is necessary. In the present work, a new method for estimating surface transport of gases based on a hybrid Monte Carlo method with unbiased random walk of tracer atom on the pore surface has been introduced. The nonoverlapping packings used in the present work were fabricated using an algorithm of very slowly settling rigid spheres from a dilute suspension into a randomly packed bed. The algorithm was modified to obtain unimodal, homogeneous Gaussian and segregated bimodal porous solids. The porosity of these solids was varied by densification using an arbitrary function or by coarsening from a highly densified pellet. The surface tortuosity for the densified solids indicated an inverted bell shape curve consistent with the fact that at very high porosities there is a reduction in the connectivity while at low porosities the pores become inaccessible or dead-end. The first passage time distribution approach was found to be more efficient in terms of computation time (fewer tracer atoms needed for the linearity of Einstein's plot). Results by hybrid discrete-continuum simulations were close to the discrete simulations for a boundary layer thickness of 5λ.

1. Introduction

The fabrication and modification of microporous zeolites (diameter < 1.5 nm) has been widely studied in the past because of its successful application in catalysis, separation, and purification of gases. Recently, there have been several inventions in the area of inorganic nanoporous materials such as MCM-41/SBA-15, hollow nanospheres, etc.[1−5] These materials are considered to be promising because of very high surface area (ca. 1000 m^2/g) and uniform/well-defined and easily tunable pore size/structure in micro-mesopore (2−30 nm) size range.[1−7] The method of synthesis varies; for example, MCM-41 are most commonly synthesized by forming a silica or alumina network around the surfactant micelles (e.g., cetyltriethylammonium bromide) and then removing the surfactant by burning it in air.[2,5,6] SBA-15[3] is made by forming a silicate network by templating it with Pluronic P123 triblock copolymer. The template is then removed by dissolving the materials in ethanol followed by calcining in air. The hollow nanospheres are made from spray pyrolysis.[4] On several occasions, these materials are subjected to higher temperatures when they are used as catalysts. Therefore, the thermal stability of the walls of these materials at higher temperature is of significant importance. It is highly desirable that these materials retain their pore size and structures at high temperature. There have been several contradicting reports in the literature on the wall structure of these materials.[7−9]

These materials are considered crystalline because of the regular arrangement of the pores; however, small-angle X-ray scattering results show that walls are not crystalline. The wide-angle X-ray scattering of these materials has indicated that the structure has an ordered range up to 8−10 Å or more (MRO, medium range order).[9] As the walls are thin (for MCM-41, wall thickness is 6−10 Å) and contain physical deformations, they may collapse on heating.[7,8,10,11,12] This is probably one of the main reasons behind the unsuccessful attempts to fabricate highly ordered alumina MCM-41.

The atomistic simulation of variable stoichiomtry metal oxides pose a significant challenge because (a) the charges of the individual aluminum and oxygen atom depend on their location and surrounding atoms, (b) variation of the local atomic structure at the interface and the bulk at the nanoscale, and (c) difficulties in the atomistic representation at the buried interface. There have been few studies addressing these problems, but none has been considered successful. Recently, Streitz and Mintmire[13] proposed a new model, ES+EAM, (Electro Static+Embedded Atom Potential) a variable charge-transfer molecular dynamics potential which has been found to be a success in modeling the metal−metal oxide interfaces as well as bulk aluminum oxide. The approach was found to be effective in describing the cohesive, structural, and elastic properties of both fcc and α-alumina.[13,14] Campbell et al.[15] extended this approach to study the oxidation of large aluminum clusters and reported that a significant charge transfer gives rise to large negative pressure in the oxide layer at 300 K. Zhou et al.[16] found that the approach

* To whom correspondence should be addressed. E-mail: shekar@nanoporous.com. Web site: http://www.nanomicrostructures.com.
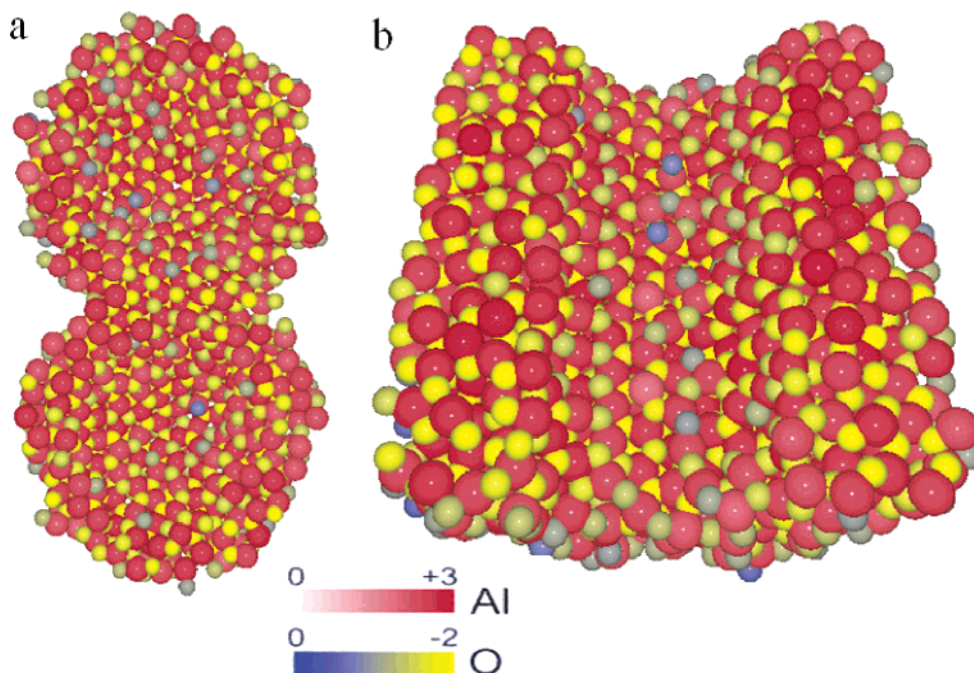
Figure 1. Cross-section view of (a) partially sintered/interconnected hollow nanosphere and (b) the nanotube. The color of the atom represents the atomic valance (for oxygen atoms: dark blue, 0; yellow, −2; whereas for aluminum: white/silver, 0; red, +3; inner diameter 3 nm and wall thickness 1 nm).

fails for alloy systems and modified it for oxidation of multimetal system such as O−Al−Zr. In this manuscript, we have used the Streitz and Mintmire approach to fabricate the nanoporous materials starting with several quantitative and stochastic models. Structures representing recently invented MCM-41 materials as well as hollow nanospheres have been simulated. We have studied their thermal stability and structural characteristics. The visualization of some of these structures is shown in Figures 1 and 2.

Transport of molecules within a porous solid can occur via any one or all of several mechanisms as shown in Figure 3. It could depend on the size, connectivity of the void space, mobility, mean free path of molecules in the gas phase and on surfaces, and the arrangement of the surfaces in providing a connected macroscopic path within the porous particles. There are several transport mechanisms, ranging from pressure-driven flow at long length and time scales to surface diffusion at small scales and short times. In this range of length and time scales, the operative processes evolve from the purely physical motion of noninteracting molecules to chemical reactions involving, in the case of surface diffusion, the sequential making and breaking of bonds between surfaces and adsorbed molecules.[17−22]

In most situations, molecule−surface collisions are typically assumed to occur without significant energy redistribution and with instantaneous desorption in a random direction. In reality, adsorption can occur, but if adsorbed species are immobile, the surface provides only a reservoir for molecules, without any contributions to steady-state diffusion rates. The pool of adsorbed molecules, however, can contribute to the apparent capacity of the system in tracer diffusivity measurements, such as those involving step or pulse chromatographic measurements or frequency response techniques. When adsorbed molecules can move, surfaces contribute a path for diffusion that adds to that provided by the void space. Application of classical techniques where gaseous diffusion alone is considered to be contributing to the total diffusion leads to incorrect estimates of gas diffusivity.[17−26] Table 1 describes few systems reported in the literature where there is a significant contribution of the

transport due to surface diffusion. For the adsorption of n-ethane, propane, and butane on porous silica of 2.2 nm pore size, the contribution of the flux due to surface diffusion amounts to 60−90%, and adsorption on carbon has 70−75% contribution. Also, for the propane adsorption on MoS_2 with a pore diameter of 1.2 nm, the surface diffusion contributes to 32% of the total flux. This clearly indicates that for a variety of micro- and mesopore systems, the flux due to surface diffusion contributes to a significant amount in the total flux.[22−26] Several experimental and theoretical studies have addressed surface and gas diffusion within porous solids, but simulations of surface diffusion on realistic pore representations have not been reported. In the present work, we have presented a new Monte Carlo model for the study of surface diffusion on a random packing.

2. Simulation Details

2.1. ES + EAM Potential. The MD simulation used in the present work employ the variable charge-transfer interaction potential developed by Streitz and Mintmire.[13] The potential is referred to as ES + EAM potential, where ES represents the long-range electrostatic interactions and EAM represents the short-range embedded-atom method interactions. The method has been discussed in detail in the literature.[13,14] The parameters used in the present work are given in Table 2.

The molecular dynamics simulations were performed using the Verlet algorithm with a time step of 1.0 fs. The starting position of the atoms in the nanospheres or tubes was chosen by a deterministic approach. The Al and O atoms were placed in the cylindrical or spherical annulus using fcc structure rules. The structures were equilibrated for about 200−300 ps at constant temperature of 300 K allowing formation and breaking of the Al−O bonds. The duration of the equilibration was varied with different structures until we obtain the structure which show small variation in temperature (5 K) when equilibrated at constant energy. Several structures with up to 10 000 atoms were fabricated in the present study. The hollow spherical structures
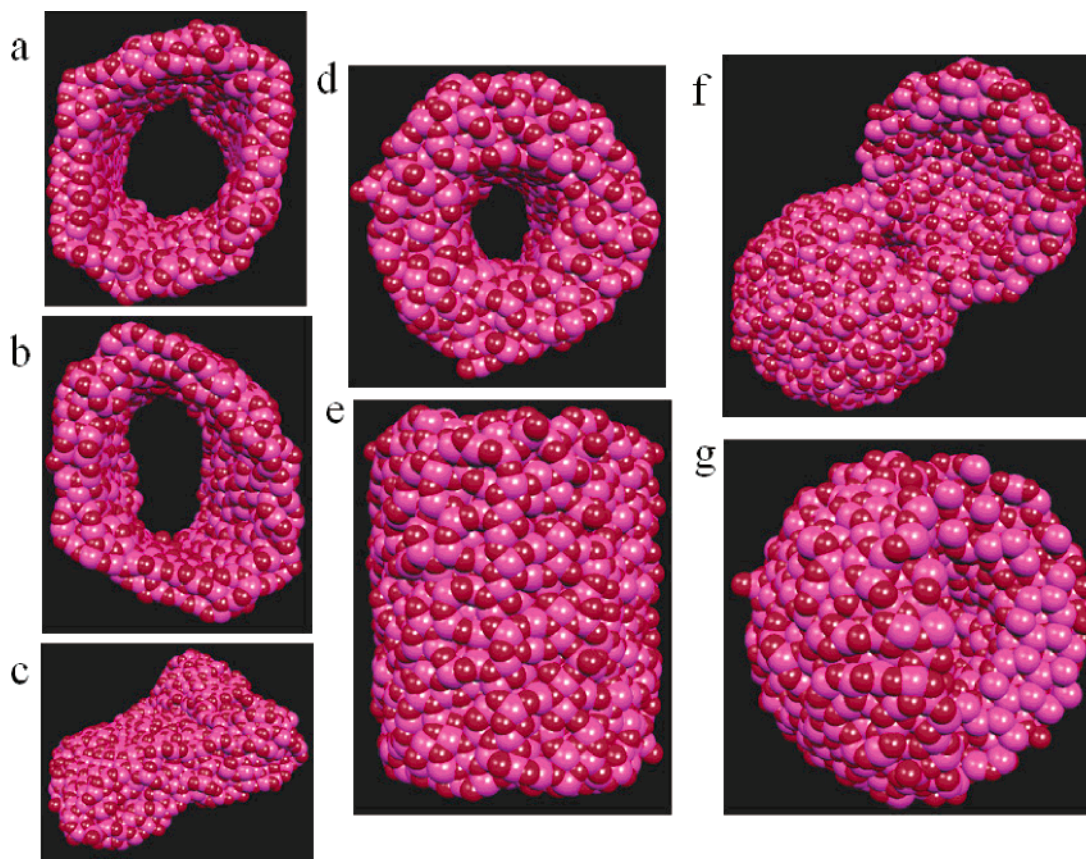
Properties of Nanostructured Materials

J. Phys. Chem. B, Vol. 109, No. 12, 2005 **5693**

Figure 2. Structure and thermal stability of the nanoporous materials. (a−c) The nanotube with 0.6 nm thin walls at 300, 500, and 1000 K, respectively. (d and e) The two different views of the same nanotube with 1 nm thick wall at 1000 K. (f and g) Cross-section of the porous spheres with 0.6 nm thick walls at 1000 K.
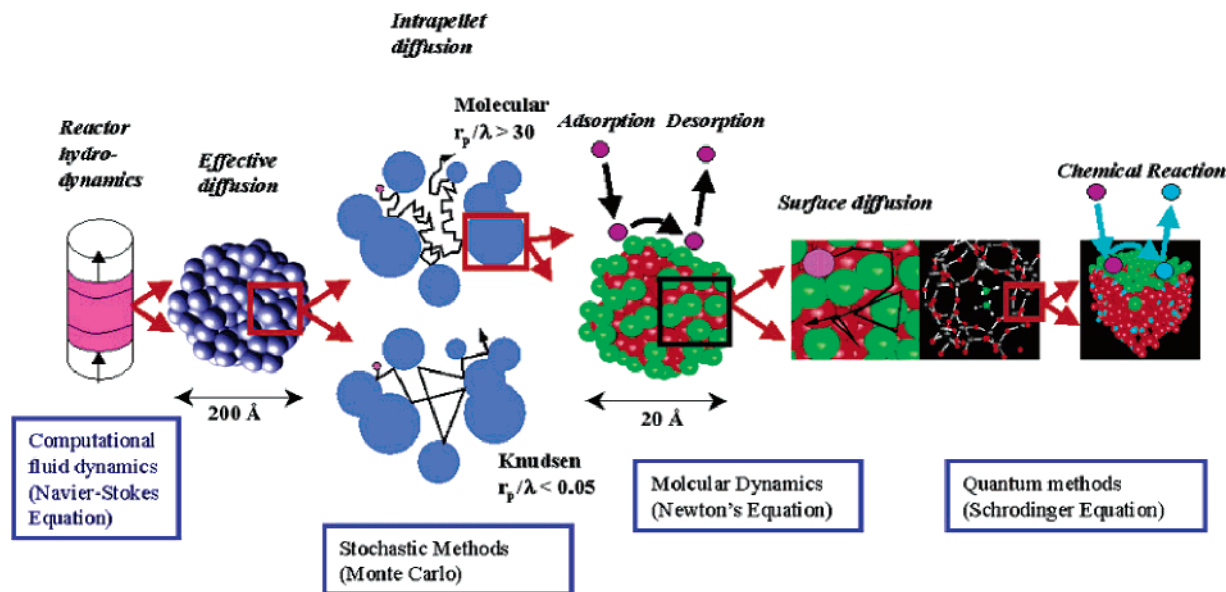

Figure 3. Summary of gas transport mechanisms at various length scales (details in section 1).

and nanotubes of different diameter in the range of 2−10 nm were also fabricated using similar approach. The wall thickness of the spheres was in the range of 0.5−2 nm. It has been reported in the literature, depending upon the method of synthesis, the the walls of these materials could be in the range of 0.5−2 nm.[2,6−8,10,11] Our choice of wall thickness is consistent with the literature.

2.2. Simulations of Pore Structure. The fabrication of the porous structure used in the present work involves sequential packing of spheres and sintering steps, which assemble a random loose aggregate of touching spheres and then overlap such spheres in order to describe changes in void fraction caused by densification or coarsening. The spheres are chosen randomly from a prescribed size distribution (unimodal, Gaussian, or bimodal), and random loose packings are constructed by dropping individual spheres at a random cross-sectional position until a three point contact is reached. Relocation of spheres by their further movement into lower positions or by movement

TABLE 1: Surface Diffusion Has Contributed Significantly to the Total Flux[a]

diffusing molecule	support material	R_p (Å)	D_s (cm^2/s)	% transport due to surface diffusion	ref
C_2H_6, C_3H_8, n-C_4H_{10}	silica	11	10^{-5}	60–90	22
C_3H_8	MoS$_2$	17	10^{-5}	32	23
CH$_4$, C_2H_6	carbon	6	10^{-6}–10^{-5}	70–75	24
n-C_6H_6	carbon	21	10^{-5}	75	25

[a] T = 298 K, P = 1 atm, amount adsorbed $\ll$ monolayer coverage.

of previously placed spheres is not allowed. This process is a realistic description of slow sedimentation and filtering of liquid slurries, from which these porous solids are typically formed.

Figure 4 shows a pictorial view of various packings fabrication studied in the present work. For simulating bimodal segregated packings, the first step involves simulation of a microsphere packing with an average diameter d_2. The packing was then sintered by coarsening or densification to the prescribed void fraction. Finally, from this packing, only those spheres were kept which lie in the solid part of another imaginary packing with macroparticle diameter d_1, (the d_2/d_1 ratio varied from 0.05 to 1). This leads to a packing of spheres having large voids, which corresponds to the space between the imaginary macrospheres as well as small voids which corresponds to the spaces between the microspheres.

The intraparticle void fraction is then varied by overlapping the intraparticle spheres by a Gaussian distribution. Densification causes spheres to pack more tightly within a smaller total volume and it reflects compression or controlled sintering methods for pellet formation. Densification is simulated by increasing the radii of each sphere (uniformly or according to a Gaussian distribution) within a random loose packing with an initial void fraction of approximately 0.05 until the desired void fractions are achieved. Coarsening preserves the initial volume of a porous pellet. It is described by using the densification algorithm above until a void fraction of 0.05 is reached and removing randomly selected spheres until the desired higher void fraction is obtained. In contrast with the densification algorithm, the coarsening procedure is not a realistic description of such physical processes, but it does lead to fewer and larger pores than in densified packing with similar void fractions, as observed experimentally in coarsened and densified solids. Typical structures constructed via these densification and coarsening methods are shown in Figure 4

2.3. Surface Diffusion. Surface diffusion involves movement of atom/molecule constrained on the surface of the spheres that form the porous structure. In the present simulations, the tracer atom is placed at a random position on the packing surface. The atom is then allowed to move one step with the stepsize λ (taken from a log-normal distribution), defined as the characteristic surface mean free path. There has been no suggestion

in the literature about the distribution of the mean free path for the surface atoms, so we have taken it as a log-normal distribution. Later, our investigation has revealed that the estimates of the diffusion coefficient are independent of the mean free path. For the movement on the same sphere, the new position of the tracer atom was obtained by using a series of Cartesian and spherical coordinate transformations. The new position on the same or new sphere was estimated by solving the equation of the imaginary sphere of radius equal to λ and equation of the spheres in the packing (see Figure 5). As the equations involved are a series of basic sphere geometry equations in Cartesian and spherical coordinates and numerical solution in situations involving three spheres, they have not been provided in the manuscript. Initially, the coordinate system was rotated by the angle θ_1 and ϕ_1 along the θ and ϕ directions respectively, where subscript 1 refers to the coordinates of the tracer atom in original spherical coordinate system. The origin was then shifted to the location of the tracer molecule. After performing the random movement, the coordinates were then back transformed to the original tracer atom position.

The distance traveled by 1000 or more tracer molecules in a given number of steps was used to estimate the surface diffusivity (D_s) from the mean square displacement ($\langle R^2 \rangle$) using the equation for Brownian motion in two dimensions $D_s = \langle R^2 \rangle / 4t$. Here, t refers to the total distance traveled by the tracer atom which is equals to the number of Monte Carlo steps times mean free path. The tortuosity of the surface phase in the porous solid is then given by $\tau_s = \phi/E_s$, where $E_s = \langle r^2 \rangle|_{pack}/\langle r^2 \rangle|_{ref}$ is the normalized surface diffusion coefficient and "pack" is the packing and "ref" is the reference material which is cylinder in the present case.

The estimates from these discrete simulations were then compared with the hybrid discrete/continuum method (described in Figure 5). In the hybrid simulations, the protective boundary layer of thickness δ within which discrete simulations are carried out is located around the intersections between spheres. Outside the boundary layer, the tracer molecule advances in a single event to a random point on the circumference of the imaginary circle that makes point contact with the nearest sphere. The boundary layer thickness δ was varied in the range from λ to 10λ in order to estimate the optimum value needed for the simulations. The value of $\delta = 5\lambda$ was found to be sufficient to reproduce the results of discrete simulations.

3. Results and Discussion

3.1. Structure and Stability of Nanoporous Materials. In the present work, the ES+ potential was used to simulate several structures (hollow spheres and nanotubes of different wall thickness, nanotubes with different length) up to 10 000 atoms. The cross-section of nanotube and partially sintered porous spheres at 300 K simulated for a total of about 180–200 ps (the structures were considered to reach the equilibrium condi-

TABLE 2: Optimized ES + EAM Potential Parameters for Aluminum and Oxygen

			Atomic Parameters			
	χ (eV)	J (eV)	ζ (Å^{-1})	Z	A (eV)	ξ
Al	0.000 000	10.328 655	0.968 438	0.746 759	0.763 905	0.147 699
O	5.484 763	14.035 715	2.143 957	0.000 000	2.116 850	1.000 000

			Pair Parameters			
	r^* (Å)	α (Å^{-1})	β (Å^{-1})	B (eV)	C (eV)	
Al−Al	3.365 875	1.767 488	2.075 016	0.075 016	0.159 472	
O−O	2.005 092	8.389 842	6.871 329	1.693 145	1.865 072	
Al−O	2.358 570	4.233 670	4.507 976	0.145 548	0.094 594	

Properties of Nanostructured Materials

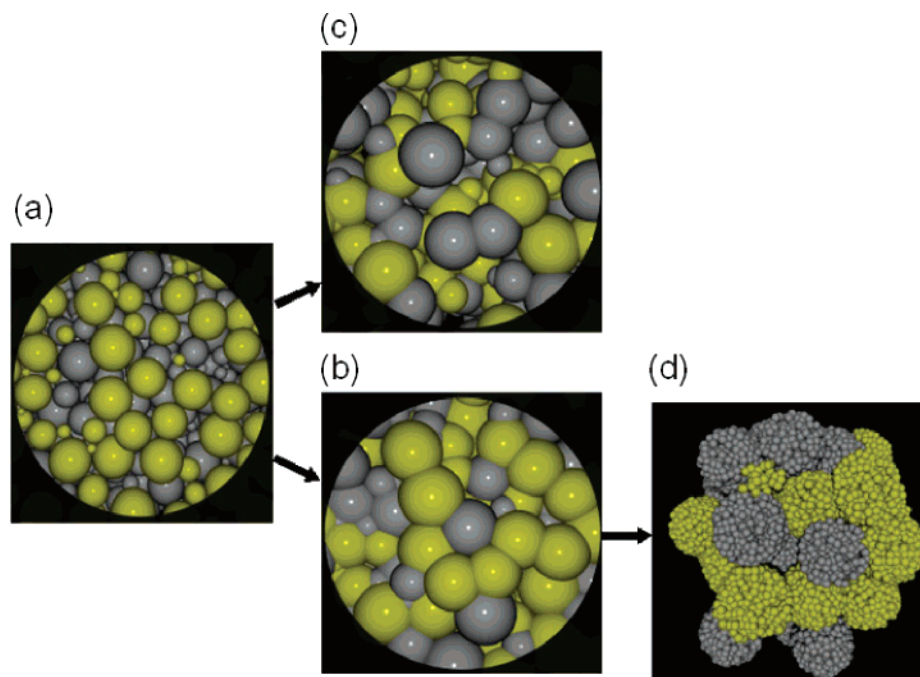*J. Phys. Chem. B, Vol. 109, No. 12, 2005* **5695**

Figure 4. Snapshot of various porous structures studied in section 2.2. (a) monosized spheres, (b) coarsened, (c) densified, and (d) bimodal porous solids.
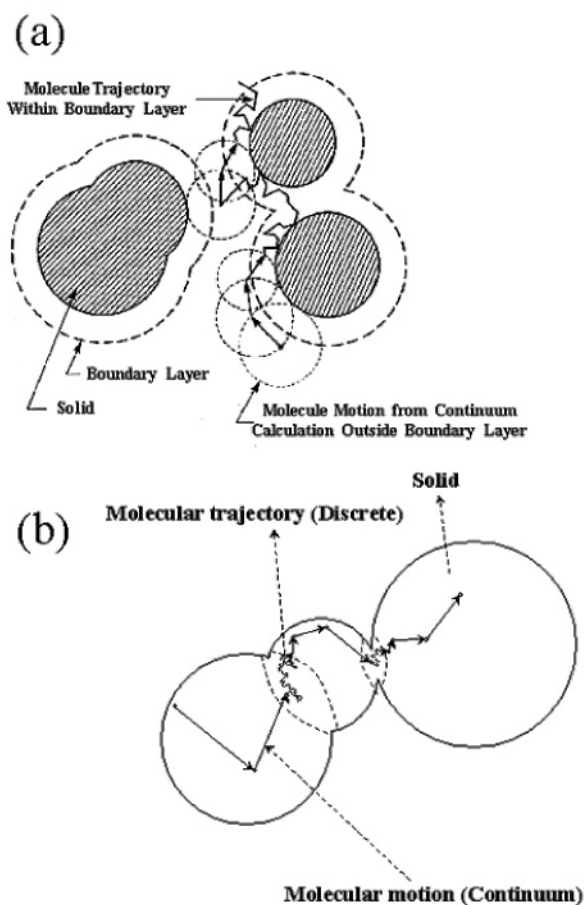

Figure 5. Schematic of hybrid discrete/continuum simulation for (a) gas phase and (b) surface diffusion. The area in the dotted line in (b) represents the place where discrete calculations were done.

tion, if for a constant energy simulations the variation in temperature of the structure was found to be less than 5−10 K) starting with a deterministic structure are shown in Figure 1. The hollow nanosphere shown in Figure 1a had an internal

radius of about 1.5 nm and a thickness of 0.6 nm. The total number of atoms was 2600. The nanotube shown in Figure 1b had a wall thickness of about 1 nm, and the total number of atoms was 3600. The color of the atom represents the atomic valance (for oxygen atoms, dark blue: 0, yellow: −2, while for aluminum, white/silver: 0, red: +3). The hollow nano-spheres were equilibrated with a stepsize of 1 fs in a simulation cell of 40 nm in diameter with elastic boundary conditions. The radius and edges of the structures were estimated from radial density and charge profile (not shown here). The averaging of the snapshots was performed until the radial density and charge profile was steady and reproducible. This was for about 100−150 ps for a typical simulation. The density of the walls is 3.9 g/cm^3 close to the density of bulk aluminum oxide 3.99 g/cm^3 (at 300 K). From the $g(r)$, the Al−Al and Al−O bond lengths for these structures were found to be 0.274 and 0.176 nm, respectively. The pair distribution function $g(r)$ determines the number of atoms surrounding a given atoms by calculating the number of atoms of each kind in hypothetical concentric spheres around that atom. The details of the procedure for estimating g(r) are provided in several text books (e.g., ref 27) The literature value of 0.18−0.19 nm for amorphous Al2O3 is little higher. The diffusion coefficient was estimated using Einstein's equation (the plot of square of displacement versus time). Diffusion coefficient of Al and O in the walls of the nanospheres as well as nanotubes was found to be ($D_{O2} = 1 \times 10^{-6}$ cm^2/s) close to the value reported in the literature[15] for the nanoclusters ($D_{O2} = 7.4 \times 10^{-5}$ cm^2/sec). In addition, the diffusivity of aluminum was found to be about 50% more than that of oxygen.

The pore structure of some of these materials at different temperatures is shown in Figures 1 and 2. The structures at 300 K was heated using a linear temperature gradient. In all of the cases, the linear temperature gradient of 1 K/ps was used for heating the structures. In one of the trial simulations, we have also tried a temperature ramp of 0.1 K/ps, and it was found that the radial density and charge distribution does not vary much. The experimental fabrication of MCM-41 involves the polymerization of silica around the surfactant liquid crystal

micelles (or block copolymers).[2,3,5−8] After that in most cases, the template is removed by burning in air. Most of the researchers use a temperature ramp of 2−3 K/min (we used about 3 K/min in our own experiments).[8] The exact simulation of synthesis of silica in a solution is difficult and requires a large computational time. It also needs information on the force fields for the micelle−alumina structure as well as properties of the micelles at higher temperatures. However, it is possible to use analogies for such a synthesis. In ongoing research in our group, we are simulating the fabrication of MCM-41 and SBA-15 resembling the actual synthesis. The first step in simulating MCM-41 materials involves the placement of rod shaped dummy atoms to represent the micelles inside the hexagonal unit cell (one full micelle at the center and 4 quarters of the micelle at the corners). The Al and O atoms are then placed in the cavity either using stochastic or quantitative approach. The structure is relaxed and equilibrated and the dummy micelle atoms are then removed from the structure. The full details of this procedure are part of another manuscript.

The effect of different heating rates on the structure is an important area of research but has not been covered in this manuscript. For the comparison purpose, we have selected 1 K/ps heating rate in all of the cases. Figure 2a−c shows the nanotube with a total of 2300 atoms having thin walls (ca. 0.5−0.7 nm) at 300, 500, and 1000 K respectively. It can be seen that, with increasing temperature, the pore structure deformation increases. At 1000 K, the pore structure of the nanotube breaks down completely. Figure 2, parts d and e, shows the nanotube of 3600 atoms and with a thicker wall (ca. 1 nm) at 1000 K. It was observed that no significant deformation of the pore structure occurs. Figure 2, parts f and g, shows the cross-section of the inverted nanospheres at 1000 K. The wall thickness of these structures is around 0.6−0.7 nm. It was observed that while heating it from 300 to 1000 K, no significant deformation of the pore structure occurs for the inverted nanospheres. The results show that the hollow nanospheres have higher thermal stability as compared to the nanotubes of the same wall thickness.

3.2. Unbiased Random Walk. To estimate the surface diffusivity, the random movement of a tracer atom on a packing surface was studied. Any possible bias in the motion of tracer molecules on packing surfaces, especially at the intersections between spheres, was probed using a packing of five partially overlapped spheres (exposed area 45−53%) as shown in Figure 6. The surface of each sphere was divided into 2500 patches using spherical coordinates. The number of sojourns that the tracer makes to each of the patches was recorded and normalized by the surface area of each patch in order to obtain the frequency with which the tracer samples each surface patch. In Figure 7, the fully exposed patches lie far from the sphere intersections, whereas those with fractional areas lie at the intersections. The results shown in Figure 7 confirm that, except for statistical fluctuations for patches too small for representative sampling, no bias is detected in the movement and crossing procedures used to describe random motion on the surface of the packing.

In addition to the packing, we also studied the unbiased movement on the surface of the cylinder. For this purpose, the cylinder surface was divided into 50 patches along the θ coordinate (in cylindrical coordinates, for $\theta = 0$ to 2π). During the trajectory of the atom, the number of visits the tracer atom made to the individual patches of this cylinder surface were counted. The visiting density, in the units of the number of visits per unit area of the cylinder, was found to be almost within 5% for all of the patches. In addition, the Einstein's plot was found
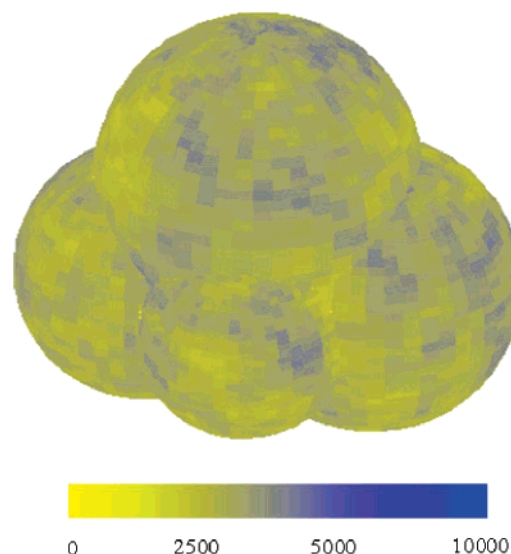

Figure 6. Visualization plot of visiting frequency for surface diffusion of a tracer atom in a model packing consisting of 4 overlapping spheres.

to be linear for various step-sizes in the range of $0.001−0.1r_c$, where r_c is the radius of the cylinder. Also, the plot of D_s/ν versus the step size was found to be linear and independent of radius of the cylinder. It appears that the surface diffusion in the cylindrical pore is analogous to the bulk diffusion in the gas phase in terms of the mathematical analysis.

3.3. Diffusion in Unimodal Porous Solids. The packings obtained from the monosize spheres were then densified using two different arbitrary functions, a uniform random distribution and a Gaussian function. The comparison of gas phase and surface tortuosity for the densified and coarsened solids is shown in Figure 7, parts a and b, respectively. The gas-phase tortuosities were obtained from the simulations in the Knudsen regime. As can be seen for both the densified and coarsened solids, τ_g is a weak function of porosity, for $\phi > 0.25$, but for larger ϕ, it increases rapidly with decreasing ϕ. At $\phi < 0.25$, more and more pores become inaccessible (completely closed) or nonconducting (dead-end). Also, the coarsened solids show slightly higher values of τ_g compared with the densified solids consistent with the fact that, when the spheres are randomly removed from a tight nonconducting packing, the probability of creating inaccessible (completely closed) or nonconducting (dead-end) pores is higher. In contrast to the gas-phase tortuosities, surface tortuosity (τ_s) values show a U shaped curve for the densified packing. The values of (τ_s) do not vary significantly over the range of $\phi = 0.2$ to 0.35 (relative change of about 10%) as compared to the changes observed for $\phi < 0.2$ and $\phi > 0.35$. The τ_s increased by about 30% when ϕ increased from 0.35 to 0.4, and also an increase of 80% was observed when ϕ decreased from 0.2 to 0.1. For $\phi > 0.25$ for the coarsened solids, τ_s is a weak function of ϕ as seen from the fact that in going from $\phi = 0.25$ to 0.4, τ_s changed only 1%. However, for $\phi < 0.25$, τ_s is a strong function of ϕ evident from the fact that in going from $\phi = 0.25$ to 1, τ_s increased by 115% (Figure 7). The behavior of the densified packing is consistent with the fact that, as the overlap between the spheres is reduced gradually, a point is reached where they are just touching each other and the probability of the tracer molecule moving from one sphere to another sphere decreases, which results in higher τ_s. Similarly, when the overlap increases gradually, more and more surface area becomes either inaccessible (completely closed) or nonconducting (dead-end). For the coarsened solids, as the spheres are randomly removed from a
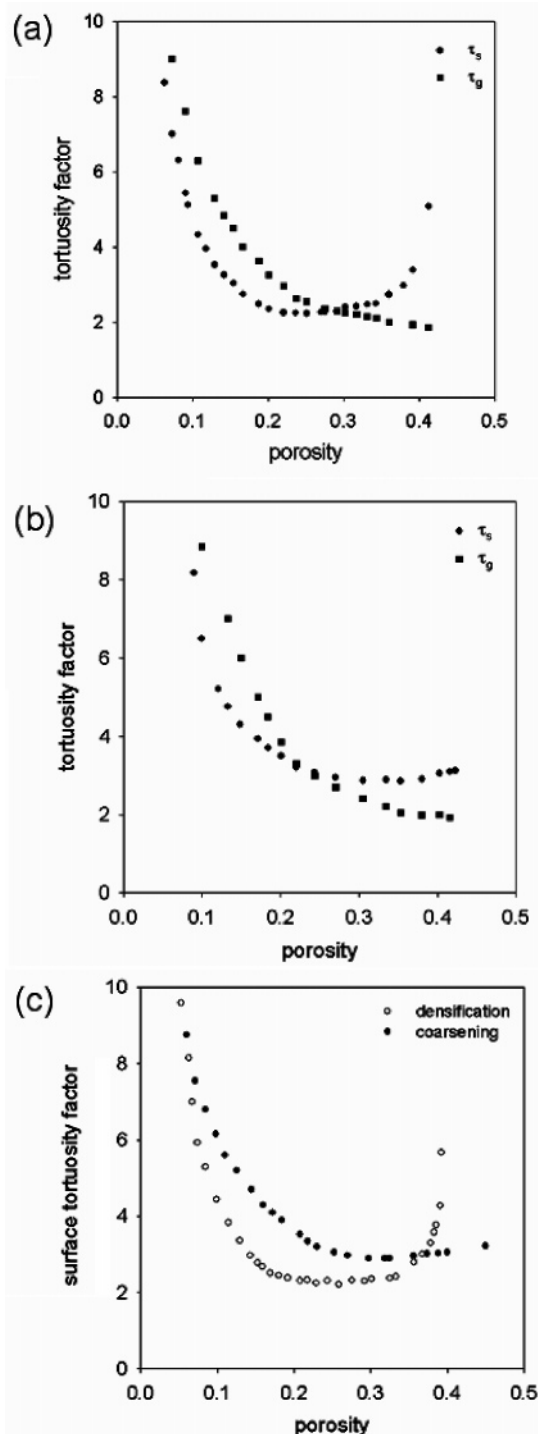
Figure 7. Surface and gas-phase tortuosity of (a) densified and (b) coarsened solids; (c) densified and coarsened solids with large variance (variance, $\sigma^2 = 2.25r^2$).

Figure 8. Pore size distribution of the (a) densified and (b) coarsened solids in terms of arbitrary units of sphere radius.

highly dense packing, the possibility of forming inaccessible (completely closed) or nonconducting (dead-end) surface is higher, which results in their higher surface tortuosity compared to the densified solids. However, the coarsened solids reach a constant value of $\tau_s = 2.9$ and do not follow the same pattern as the densified solids for $\phi > 0.3$. This is consistent with the fact that even at $\phi > 0.3$, as the process of removal of spheres is random, many aggregates of spheres exist which have much higher connectivity than that observed in the densified solids. We also found that the packing fabricated using another arbitrary function has no significant effect on the tortuosities except at ϕ
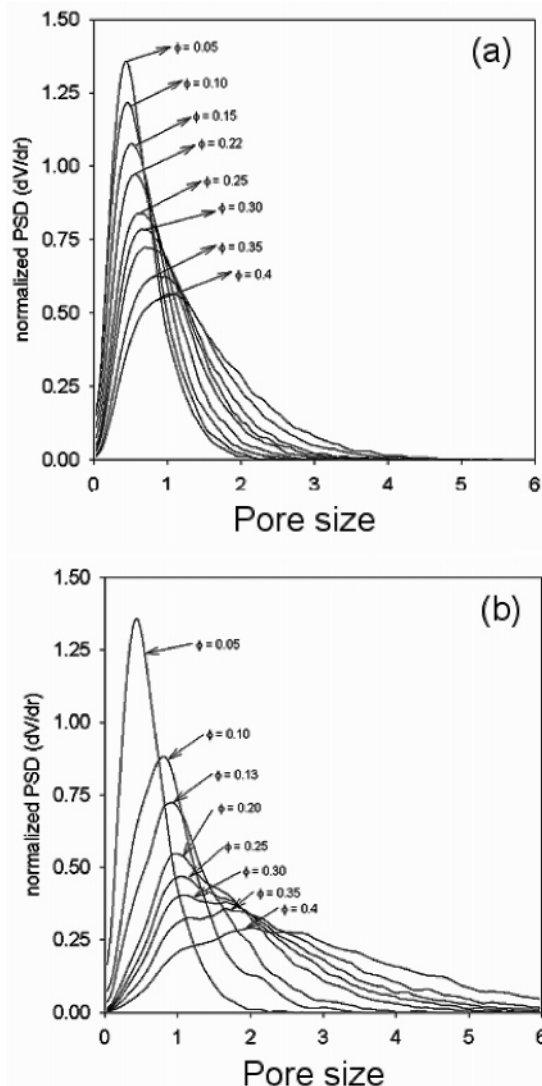
> 0.35 and $\phi < 0.1$, where the packings fabricated using Gaussian distribution function had slightly higher values compared to those made from uniform distribution function.

The estimates of τ_s were always lower than τ_g for the densified solids for ϕ less than about 0.28 with the difference between them increased with decrease in porosity. At $\phi \sim 0.28$, the gas and surface tortuosities are equal ($\sim$2.2) but at higher porosities, the surface tortuosity was higher than the gas tortuosity. Also, with increasing ϕ, the value of τ_g reached a steady value of about 2 while τ_s increased steadily. The absolute value of difference in τ_g and τ_s at $\phi = 0.1$ and 0.4 was 31 and 110%, respectively, as shown in Figure 7. For the coarsened solids, the gas phase and surface tortuosities are equal ($\sim$3.2) at $\phi \sim 0.22$. With either decrease or increase in the porosity, the variation in the tortuosity is significant, as evident from the result that, for $\phi \sim 0.1$ and 0.4, the absolute percentage difference between the tortuosities is 26 and 56% respectively as shown in Figure 7. A plot of pore size distribution of the densified and coarsened solids obtained by the simulation technique is shown in Figure 8. With increase in the porosity, the mean pore size (units of sphere radius) as well as the breadth of the distribution increases for both the solids. The coarsened solids have a broader distribution as compared to the densified solids.
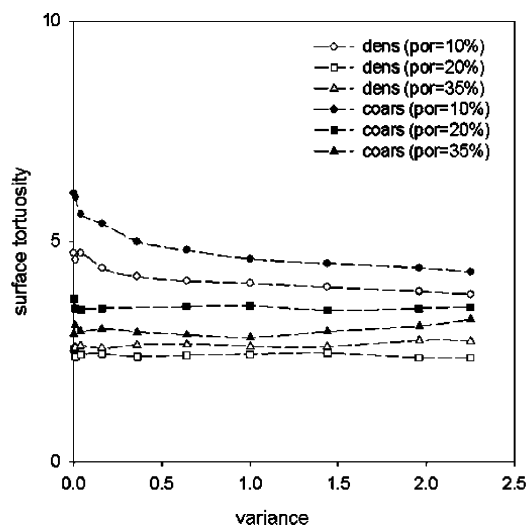
Figure 9. Surface tortuosity of the tracer atom as a function of variance of distribution of the packing.

The results of variation of τ_g and τ_s with ϕ of the packings made from the spheres distributed according to the Gaussian distribution are shown in Figure 7c. The nonoverlapping packings were then densified using a Gaussian distribution function to obtain a desired porosity. The values of τ_s were found to increase by 2% (from 2.28 to 2.33), whereas τ_g decreased by 5% (from 2.23 to 2.12) when changing from a monosize to a broad distribution packing (variance, $\sigma^2 = 2.25$). However, the gradient of variation of τ_s and τ_g are different at different ϕ for both the solids. The effect of variance of the Gaussian distribution on the surface and gas of the densified and coarsened solids as different porosities was also studied. At lower porosities (~ 0.1), τ_s decreases with increasing variance of the distribution significantly evident from the results that τ_s decreased by 21% when the variance of the radius was increased from 0 (monosize) to 2.25 (broad). Correspondingly, the coarsened solids also show a decrease 30% in the same range. However, for higher porosities (> 0.2), the estimates of τ_s do not change significantly over the entire range of the variances studied here.

The porous structures made from spheres with large variance ($\sigma^2 = 2.25$) in distribution of radius by Gaussian distribution were also studied. The variation of τ_s with ϕ for the densified and coarsened solids is shown in Figure 9. For the densified solids, τ_s decreased sharply with increase in ϕ for $\phi < 0.2$ after that it remained almost constant for $\phi = 0.2-0.3$ ($\tau_s = 2.3$) and then it increased sharply for $\phi > 0.3$. The coarsened solids followed a similar pattern where τ_s decreased sharply with increase in ϕ for $\phi < 0.2$, it remained almost constant for $\phi > 0.25$. It should be noted here that for $\phi < 0.1$ the packings made from monosize spheres had larger τ_s while the opposite trend was observed for $\phi > 0.35$. Packings made by densification of monosize spheres always had higher values of τ_s, with the difference increased with decreasing ϕ. The surface tortuosity of both the coarsened and densified solids at $\phi \sim 0.38$ is $\tau_s \sim 3.6$.

The comparison of τ_g for the coarsened solids made from monosize spheres and spheres with variance equals 2.25 (units of mean sphere radius) over the range of $\phi = 0.06-0.4$ indicated that both solids have the same τ_g at $\phi = 0.4$. The difference between the two increases with decreasing porosity. For $\phi = 0.07$, the packings made from monosize spheres had 20% larger τ_g compared to the packing made from spheres with $\sigma^2 = 2.25$. The corresponding estimates of τ_s indicated that the values of τ_s for both solids is same and almost constant for $\phi = 0.25-$

0.4. Also, the difference increases with decreasing porosity. At $\phi = 0.072$, τ_s for the packing made from monosize sphere was 35% larger than the one made from the spheres with $\sigma^2 = 2.25$. The surface and gas tortuosity results for the packings made from monosize spheres and densified using a narrow Gaussian distribution function were similar to the packings made from monosize spheres and densified using a broad Gaussian distribution function.

3.4. Study of Other Parameters. It is expected that the stepsize does not have any effect on the tortuosity. For the packings with $\phi = 0.06-0.4$, the estimates of τ_s for $\lambda/\bar{r}_p$ of 0.1 and 0.01 were found to be within 1%. This indicated consistency of the present simulation technique in estimating τ_s. However, computation time increased significantly for larger values of $\bar{r}_p/\lambda$. In contrast to the estimates of τ_s, the values of τ_g for the Knudsen and the Bulk regime were significantly different from the transition regime. As described earlier, it was possibly due to the inadequacies of the Bosanquet equation to define the diffusivity in the transition regime given that the pore structure studied in the present work consisted of noncylindrical pores, which vary in shape, size, and connectivity. The results obtained here indicate that our choice of $\lambda/\bar{r}_p = 0.1$ (for τ_s) and $\bar{r}_p/\lambda = 0.01$ (for τ_g) were sufficient to describe the tortuosity of the packings studied.

The first passage time distribution (FPT) method is widely used in estimation of diffusion coefficient from Monte Carlo simulations.[28] In FPT approach, time steps required for several tracers to reach a certain distance in the first attempt is collected and averaged. The mean value of $\langle r^2 \rangle$ estimated by such method is the used to estimate the diffusion coefficient. The FPT approach was compared with the conventional averaging method (where the distance traveled by the tracer molecule is averaged for each time interval) for the estimates of τ_s. The FPT approach was found to be more efficient in terms of computation time (as it needed fewer tracer atoms to obtain a linear plot of $\langle r^2 \rangle$ versus time steps. For the FPT approximation, about 600−800 molecule gave good statistics, compared to about 1000−2000 needed for the conventional averaging method to achieve the same statistics. In addition, the Einstein plot (plot of $\langle R^2 \rangle$ versus time) was found to be linear over a larger range of R^2 for the FPT method. The estimates of τ_s by the discrete and hybrid simulations for a few packings studied over the range $\phi = 0.1-0.35$ were found to be same. For the bulk regimes, the FPT was found to over-predict τ_g. The boundary layer thickness of $\delta = 5\lambda$ was found to be sufficient for estimation of both τ_g and τ_s. For $\delta > 5\lambda$, computation time increased, whereas for $\delta < 5\lambda$, the computation time decreased but the estimates were less accurate.

3.5. Bimodal Solids. To change the total porosity of the segregated bimodal solids, a systematic variation of macropellet porosity, ϕ_{Macro}, and local porosity, ϕ_{micro}, was performed. ϕ_{Macro} is the porosity of the solids when the macrospheres are nonporous, whereas ϕ_{micro} is the porosity within the macrosphere when it is porous. As seen from Figure 10, τ_s increases with increasing ϕ_{Macro}, with each curve showing an inverted bell shape. The packings presented in Figure 10 were obtained for $d_2/d_1 = 10$ and radii of the nonporous macrospheres as well as the microspheres before the fabrication followed a Gaussian distribution. Both the microspheres as well as macrospheres used for the fabrication of the porous structure were densified using a Gaussian distribution to obtain a desired porosity. As ϕ_M increases, the connectivity of the macrospheres decreases and although tracer atom can move within the individual macrospheres, it requires longer path to cross from one macrosphere
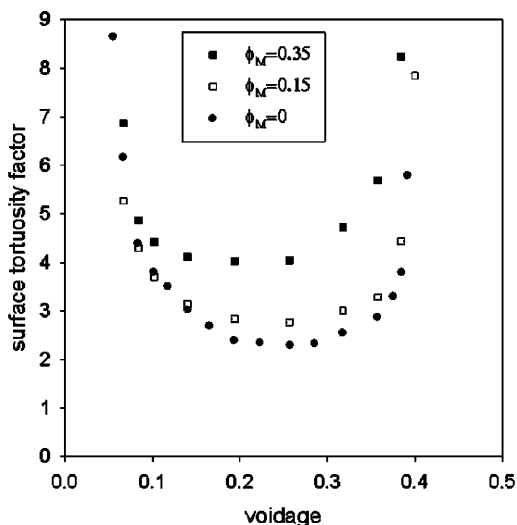
Properties of Nanostructured Materials

J. Phys. Chem. B, Vol. 109, No. 12, 2005 **5699**

Figure 10. Surface tortuosity of a bimodal solid for various macroporosities. The *Y* axis represents the voidage of micropores.

to other. Also, the tracers spent time in reaching the surface of the macrosphere and retracing its path back into the center of the macrosphere. It should be noted that the movement of the atom on the packing was not terminated if it reached the surface of the individual macrospheres. However, if the atom reached the edge of the spherical bed (made from several macrospheres), then the movement was terminated. The total exposed surface of the microspheres on the edge of the macrospheres in the packing is larger for packings with larger ϕ_{Macro}. The surface tortuosity was also studied for bimodal segregated solids fabricated from the monosize spheres (both microspheres as well as macrospheres were densified using a Gaussian distribution function to obtain a desired porosity). All of the tortuosity results follow the same pattern for variation of τ_s with ϕ_{micro} and ϕ_{Macro} compared with the surface tortuosity for packings fabricated from broad sphere size distribution.

4. Conclusion

In the present work, the deterministic models along with molecular dynamics technique with the variable charge transfer potential were used to fabricate alumina nanotubes and inverted porous solids (hollow interconnected nanospheres also called swiss cheese solids). These nanostructures resemble recently invented MCM-41/SBA-15 and the other ordered nanoporous materials. The structure and thermal stability of these materials were investigated, and it was found that the nanoporous hollow spheres have more thermal stability as compared to the porous nanotubes. Also, the nanotubes with a thick pore wall have more thermal stability. A new method of the unbiased random walk of a tracer atom on the surface of a porous structure was successfully applied to study the surface tortuosity. The gas as well as surface tortuosity values of the coarsened solids were

higher than that for densified solids. The increase in the breadth of distribution has an insignificant effect on the surface tortuosity ($\sim$2%) and gas-phase tortuosity ($\sim$5%) when changing from a monosize to a broad distribution with variance of 2.25 for the porosity of 0.27. With the boundary layer thickness of $\delta = 5\lambda$, the hybrid discrete-continuum simulations were able to give accurate estimates of both surface and gas-phase tortuosities in comparison to the discrete simulations. The FPT approximation was efficient over the conventional averaging method in terms of computational time and the statistics of the results.

References and Notes

(1) Imhof, A. *Nature* **1997**, *389*, 948.
(2) Kresge, C. T.; Leonowicz, M. E.; Roth, W. J.; Vartuli, J. C.; Beck, J. S. *Nature* **1992**, *359*, 710.
(3) Zhao, D.; Huo, Q.; Feng, J.; Chmelka, C. F.; Stucky, G. *J. Am. Chem. Soc.* **1998**, *120*, 6024.
(4) Kim, S. H.; Liu, B. Y. H.; Zachariah, M. R. *Langmuir* **2004**, *20*, 2523.
(5) Corma, A. *Chem. Rev.* **1997**, *97*, 2373.
(6) Sonwane, C. G.; Bhatia, S. K. *J. Phys. Chem. B* **2000**, *104*, 9099.
(7) Edler, K. J.; Raynolds, P. A.; White, J. W.; Cockson, D. *J. Chem. Soc., Faraday Trans.* **1997**, *93*, 199.
(8) Sonwane, C. G.; Bhatia, S. K.; Calos, N. *Ind. Eng. Chem. Res.* **1998**, *37*, 2271.
(9) Pophal C.; Fuess, H. *Microporous Mesoporous Mater.* **1999**, *33*, 241.
(10) Sonwane, C. G.; Bhatia, S. K. *Langmuir* **1999**, *15*, 2809.
(11) Sonwane, C. G.; Bhatia, S. K.; Calos, N. *Langmuir* **1999**, *15*, 4603.
(12) Gregg, S. J.; Sing, K. S. W. *Adsorption Surface Area and Porosity*; Academic Press: New York, 1982.
(13) Streitz, F. H.; Mintmire, J. W. *Phys. Rev. B* **1994**, *50*, 11996.
(14) Keffer, D. J.; Mintmire, J. W. *Int. J. Quantum Chem.* **2000**, *80*, 733.
(15) Campbell, T.; Kalia, R.; Nakano, A.; Vashishta, P.; Ogata, S.; Rodgers, S. *Phy. Rev. Lett.* **1999**, *82*, 4866.
(16) Zhou, X. W.; Wadley, H. N. G.; Filhol, J.-S.; Neurock, M. N. *Phys. Rev. B* **2004**, *69*, 035402.
(17) Ruthven, D. M. *Principles of Adsorption and Adsorption Processes*; Wiley: New York, 1984.
(18) Do, D. D. *Adsorption Analysis: Equilibria and Kinetics*; Imperil College Press: London, 1998.
(19) Park, I.-S.; Do, D. D.; Rodrigues, A. E. *Catal. Rev.-Sci. Eng.* **1996**, *38*, 189.
(20) Kapoor, A.; Yang, R. T.; Wong, C. *Catal. Rev.-Sci. Eng.* **1989**, *31*, 129.
(21) Heynes, H. W. *Catal. Rev.-Sci. Eng.* **1988**, *30*, 563.
(22) Schneider, P.; Smith, J. M. *AIChE J.* **1968**, *14*, 886.
(23) Reed, E. M., Jr.; Butt, J. B. *J. Phys. Chem.* **1971**, *75*, 133.
(24) Costa, E.; Calleja, G.; Domingo, F. *AIChE J.* **1985**, *31*, 982.
(25) Kapoor, A.; Yang, R. T. *Chem. Eng. Sci.* **1991**, *46*, 1995.
(26) Reyes, S. C.; Iglesia, E. *J. Catal.* **1991**, *129*, 457.
(27) Allen, M. P.; Tildesley, D. J. *Computer Simulation of Liquids*; Oxford University Press: New York, 1989.
(28) Siegel, R. A.; Langer, R. *J. Colloid Interface Sci.* **1986**, *109*, 426.